Chinese Chemical Letters 37 (2026) 111268

Contents lists available at ScienceDirect

Chinese Chemical Letters

journal homepage: www.elsevier.com/locate/cclet

Bulk anomalous photovoltaic induced pyro-phototronic effect in lead-free chiral perovskite for enhanced self-powered photodetection

Xin Dong[a,b], Zhijin Xu[a,b], Jing Liang[a], Tianqi Chen[a], Junhua Luo[a,b,c], Lina Li[a,b,c,*]

[a] State Key Laboratory of Structure Chemistry, Fujian Institute of Research on the Structure of Matter, Chinese Academy of Sciences, Fuzhou 350002, China
[b] University of Chinese Academy of Sciences, Chinese Academy of Sciences, Beijing 100039, China
[c] Fujian Science & Technology Innovation Laboratory for Optoelectronic Information of China, Fuzhou 350002, China

ARTICLE INFO

Article history:
Received 15 February 2025
Revised 22 April 2025
Accepted 27 April 2025
Available online 27 April 2025

Keywords:
Lead-free
Chiral-polar hybrid perovskites
Bulk anomalous photovoltaic effect
Pyro-phototronic effect
Self-powered photodetection

ABSTRACT

The bulk anomalous photovoltaic effect (BAPV) in non-centrosymmetric materials can produce photovoltage exceeding the bandgap, distinguishing them from traditional semiconductors and offering substantial potential in photovoltaics. Chiral hybrid perovskites, characterized by asymmetric structure and structural tunability, present promise to generate BAPV with desired optoelectronic properties. Herein, we introduced chiral (*S*)- and (*R*)-α-methylbenzylamine (*S*/*R*-α-MBA) cations to construct a pair of lead-free chiral-polar perovskites, denoted as (*S*-α-MBA)$_4$Bi$_2$I$_{10}$ and (*R*-α-MBA)$_4$Bi$_2$I$_{10}$ (**1*S*** and **1*R***). Remarkably, **1*S*** and **1*R*** exhibited the distinctive BAPV effect with an impressive photovoltage of 15 V, highlighting the potential for prominent photovoltaic performance. Furthermore, self-powered broadband photoresponse is realized *via* photo-induced pyroelectricity based on inherent spontaneous polarization in **1*S*** and **1*R***. The fabricated photodetectors demonstrated enhanced photocurrent response compared to those relying on the photovoltaic effect alone. This innovation eliminates the confinement of photodetection by material semiconductor properties, thereby effectively broadening their application scope.

© 2026 Published by Elsevier B.V. on behalf of Chinese Chemical Society and Institute of Materia Medica, Chinese Academy of Medical Sciences.

Non-centrosymmetric materials, lacking structural spatial inversion symmetry, exhibit various properties including ferroelectricity [1,2], piezoelectricity [3,4], pyroelectricity [3,5,6], and frequency-doubling effect [7]. Particularly, asymmetric single-phase compounds can also generate stable photocurrents and above-bandgap photovoltages under continuous uniform illumination [8,9], known as the bulk anomalous photovoltaic (BAPV) effect, which is anticipated to achieve a high-performance self-powered photoelectric response [10–12]. Currently, the exploration of BAPV has largely focused on a few insulating inorganic oxides like $LiNbO_3$ [13,14], $BaTiO_3$ [15–17], and $BiFeO_3$ [18,19]. However, the majority of these devices suffer from poor electronic properties which limit their application in the field of photovoltaics. Fortunately, the proposition of the pyro-phototronic effect aims to enhance photoelectric performance by naturally connecting the photo-induced pyroelectric effect with semiconductor properties [20–23]. The charges generated by photo-induced pyroelectric polarization can efficiently modify carrier separation and transportation. Upon light illumination, the transient temperature rises in these materials can generate current signals in the polarization direction to enhance the light response. Therefore, the exploration of novel non-centrosymmetric materials with BAPV effect accompanied by pyro-phototronic effect is desirable.

Organic–inorganic halide perovskites have become mainstream semiconducting materials with wide-ranging applications, including photovoltaics [24], light-emitting devices [25], and photodetectors [26,27]. Furthermore, the flexibility of the perovskite structures enables the incorporation of chiral ligands, giving rise to a novel concept known as chiral hybrid perovskites (CHPs) [28,29]. As a consequence, by combining the advantages of the perovskite structure with inherent chiral features, CHPs are widely used in chiral optoelectronic devices, such as spintronic devices, nonlinear optics devices and circularly polarized light detectors [30,31]. Given the unique properties, introducing chiral organic cations disrupts spatial inversion symmetry, opening avenues for high-performance photovoltaic applications. For instance, previously reported chiral perovskites, such as (*R*/*S*-1-phenylpropylamine)$_2$BiI$_5$ (0.63 V) [32], (*R*/*S*-1-phenylpropylamine)EAPbCl$_4$ (0.5 V) [33], and (*R*-β-methylphenethylammonium)$_4$AgBiI$_8$ (0.36 V) [34], have fully exhibited their fascinating bulk photovoltaic effect. On the other hand, the introduction of chiral cations renders CHPs more likely to

* Corresponding author at: State Key Laboratory of Structure Chemistry, Fujian Institute of Research on the Structure of Matter, Chinese Academy of Sciences, Fuzhou 350002, China.
E-mail address: lilina@fjirsm.ac.cn (L. Li).

https://doi.org/10.1016/j.cclet.2025.111268
1001-8417/© 2026 Published by Elsevier B.V. on behalf of Chinese Chemical Society and Institute of Materia Medica, Chinese Academy of Medical Sciences.



Scheme 1. Schematic illustration of the growth processes of **1*S*** and **1*R*** crystals.

crystallize in five chiral-polar point groups, namely C_1, C_2, C_3, C_4, and C_6 [28,35,36]. These chiral-polar perovskites with inherent polarization will readily generate the pyro-phototronic effect [37,38].

Herein, we synthesized a pair of zero-dimensional (0D) bismuth-based CHPs (*S*-α-MBA)$_4$Bi$_2$I$_{10}$ and (*R*-α-MBA)$_4$Bi$_2$I$_{10}$ (**1*S*** and **1*R***), by assembling chiral methylbenzylamine (*S*/*R*-α-MBA) cations. These compounds crystallized in the chiral-polar point group ($P2_1$), induced by the organic chiral ligands. Remarkably, the intrinsic asymmetric structure of these compounds gives rise to a notable BAPV effect, characterized by a steady-state photovoltage (V_{oc}) reaching an impressive 15 V. The synergism of BAPV and pyro-phototronic effects can further modulate the optoelectronic processes, enabling highly enhanced self-powered detection based on CHPs. These merits enable **1*S*** and **1*R*** to exhibit a broadband response range that surpasses the inherent bandgap limitation, spanning from 405 nm to 785 nm. The photodetector can realize simultaneous multi-signal sensing and effectively utilize the electric energy generated by photo-thermal coupling, opening up possibilities for the design and development of prominent self-powered materials.

Single crystals of **1*S*** and **1*R*** with a size up to $10 \times 5 \times 5\,mm^3$ have been successfully grown using the temperature-lowering crystallization method. Scheme 1 provides schematic illustrations for the crystal growth process. Powder X-ray diffraction (XRD) analysis confirmed the high purity by closely matching the simulation results (Fig. S1 in Supporting information). Furthermore, the thermogravimetric analysis revealed no mass loss from the crystals up to 495 K, disclosing its high thermostability (Fig. S2 in Supporting information). The crystallization of **1*S*** and **1*R*** is largely dependent on the addition of chiral components. These crystals adopted a chiral-polar space group of $P2_1$ (detailed crystallographic data are provided in Table S1 in Supporting information). Their chiral-polar characteristic was confirmed through the second harmonic generation signals (Fig. S3 in Supporting information). Given the similarity between the crystallographic structural parameters of the two enantiomers, the crystal structure of **1*R*** will be described in detail.

Fig. 1a illustrates the structural arrangement, comprising four *R*-MBA$^+$ cations and one $[Bi_2I_{10}]^{4-}$ dimer as the fundamental structural unit. Each $[Bi_2I_{10}]^{4-}$ anionic dimer is formed by BiI_6 octahedra sharing their edges through two iodine atoms. The chiral organic molecules are firmly anchored to iodine atoms of dimers *via* N-H···I hydrogen bonds. Moreover, the Bi-I bond lengths and I-Bi-I bond angles are 2.92−3.33 Å and 84.56°−177.30°, indicating the tilts and distortion of the inorganic skeleton (Fig. 1b, Tables S2 and S3 in Supporting information). The electric polarization (P_s) of **1*R*** primarily arises from the arrangement of the electric dipole moments of the organic cation [28]. The dipole moment of the *S*/*R*-α-MBA ion is estimated to be 7.75 Debye by DFT (Fig. S4 in Supporting information). Then, the calculated P_s along the *b*-axis was found to be $0.4\,\mu C/cm^2$ using the point charge model (Tables S4 and S5 in Supporting information). Thus, this chiral polarity feature empowers **1*S*** and **1*R*** with considerable potential to display the BAVE effect for self-driven detection.

The optical properties of **1*S*** and **1*R*** were investigated first. The ultraviolet-visible absorption spectra reveal they present a sharp

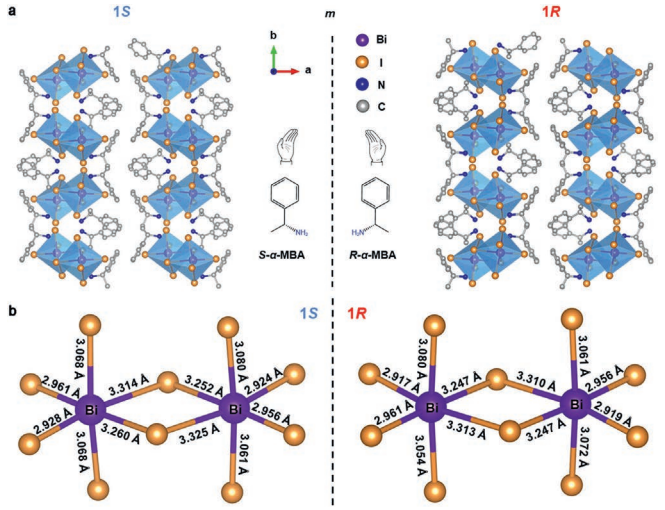


Fig. 1. (a) Structures of **1*S*** and **1*R*** crystals. (b) The inorganic frameworks and bond lengths of **1*S*** and **1*R***.

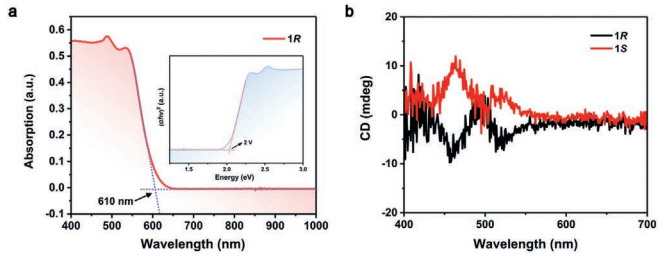


Fig. 2. (a) The absorption spectrum and optical bandgap from the Tauc plot of **1*R***. (b) The CD spectra of **1*S*** and **1*R*** films.

absorption edge at around 610 nm (Fig. 2a and Fig. S5 in Supporting information). By fitting the Tauc curve, the optical bandgap (E_g) was calculated to be 2.0 eV [39]. This value is comparable to that of other 0D binuclear bismuth halide perovskites, such as (*R*/*S*-1-phenylpropylamine)$_2$BiI$_5$ (2.17 eV) and (*R*-1-(4-fluoro)-phenylethylammonium)$_4$Bi$_2$I$_{10}$ (2.09 eV) [32,40]. Such a relatively narrow bandgap holds the potential for achieving broadband optoelectronic detection. To verify the intrinsic chirality of **1*S*** and **1*R*** crystals, circular dichroism (CD) signals were recorded for the thin films (Fig. 2b). The prepared films also show a preferred orientation of the (100) plane (Fig. S6 in Supporting information). Notably, the CD spectra exhibit that the CD signals of **1*S*** and **1*R*** are mirror images of each other and correspond to the optical intrinsic absorption of perovskites. These results provide compelling evidence of the intrinsic chirality feature of the crystals, further confirming the efficient transfer of chirality from organic molecules to inorganic parts.

Subsequently, we fabricated photodetectors using both **1*S*** and **1*R*** chiral crystals to investigate the photovoltaic effect. Under 405 nm laser illumination, the current-voltage (*I*–*V*) curves clearly showed the BAPV effect when the electrode direction was aligned parallel to the polar *b*-axis, as depicted in Fig. 3a. In this configuration, the V_{oc} impressively reached a maximum of 15 V, approximately 7.5 times larger than its optical bandgap. Particularly, the V_{OC} of **1*R*** increases with incident light intensity (Fig. S7 in Supporting information). Such a huge V_{oc} should be the first demonstration in the CHPs, much higher than that of double perovskite (4-bromobenzylammonium)$_2$CsAgBiBr$_7$ (3.2 V) and hybrid perovskite ferroelectrics (*n*-hexylammonium)$_2$(ethylammonium)$_2$Pb$_3$Br$_{10}$ (7.4 V) [10,11]. Crucially, the BAPV effect is intricately connected

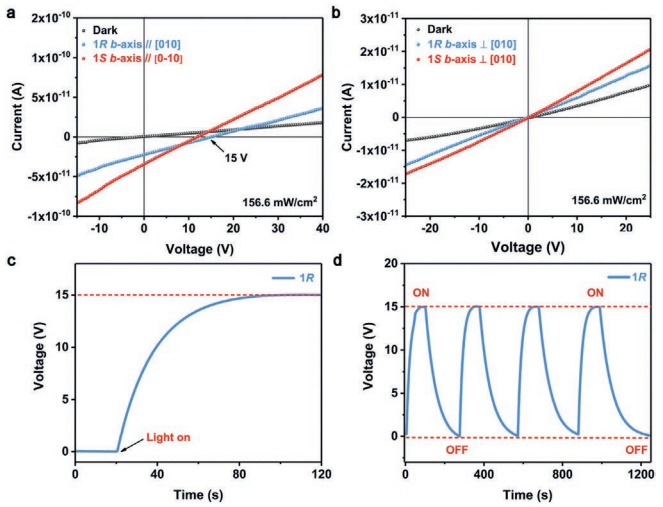


Fig. 3. (a) *I-V* curves at 405 nm laser for devices **1*S*** and **1*R***. (b) *I-V* curves for **1*S*** and **1*R*** devices when the electrode direction is vertical to the *b*-axis. (c) The V_{OC} of **1*R*** *versus* the time when the light is turned on. (d) Variation of V_{OC} with the switching "on/off" cycles.

to the P_s of the crystals. The V_{oc} and short-circuit photocurrent (I_{sc}) are observed for the opposite P_s direction: $I_{sc} < 0$ and $V_{oc} > 0$ for **1*R*** (*b*-axis//[010]) and $I_{sc} < 0$, $V_{oc} > 0$ for **1*S*** (*b*-axis//[0$\bar{1}$0]). These opposing electric polarizations between enantiomers result from the crystallographic constraints imposed by the chiral polar system. To verify polarity dependency, the crystal was rotated 180° around the *b*-axis. This resulted in a reversal of the V_{oc} and I_{sc} signs (Fig. S8 in Supporting information): $I_{sc} > 0$, $V_{oc} < 0$ for **1*R*** (*b*-axis//[0$\bar{1}$0]) and $I_{sc} > 0$, $V_{oc} < 0$ for **1*S*** (*b*-axis//[010]). Because of the chirality remained unchanged, the sign change of I_{sc} may be explained by the change of P_s direction.

To clarify the correlation between P_s and the BAPV effect, we measured photocurrents perpendicular to the *b*-axis. As expected, there are no I_{sc} and V_0 signals (Fig. 3b). This result strongly suggests that the BAPV effect is intricately linked to polarity along the *b*-axis. In other words, the photovoltaic effect, as manifested solely along the *b*-axis, reaffirms its origin in the chiral-polar character of these crystals. Fig. 3c and Fig. S9 (Supporting information) illustrate the photovoltaic-time (*V-t*) curve under continuous irradiation, exhibiting above-bandgap $V_{oc} = 15$ V in **1*S*** and **1*R***. Additionally, the *V-t* curve measured at zero bias during the light switching on/off cycles verified the good stability of the BAPV effect (Fig. 3d). The remarkable BAPV effect, independent of bandgap, highlights **1*S*** and **1*R*** as promising candidates for prominent pyro-phototronic detection.

In pyro-phototronic devices, the simultaneous operation of pyroelectric and photovoltaic effects synergistically promotes the transport of photogenerated carriers and reduces the recombination rate of electron-hole pairs [22,41,42]. The principle is illustrated in Fig. 4a. When exposed to light, charge carriers are generated within the chiral-polar structure, while the increased temperature of the **1*R*** crystal induces pyroelectric polarized potential. The transient current and four-stage behavior reveal the pyro-phototronic effect (Fig. 4b) [43]. In stage 'I', the pyroelectric material undergoes a transient current peak characterized by a sudden increase in temperature ($dT/dt > 0$). This current comprises both the output current from the pyroelectric and photovoltaic effects, represented as $I_{pyro+photo}$. Under continuous illumination,

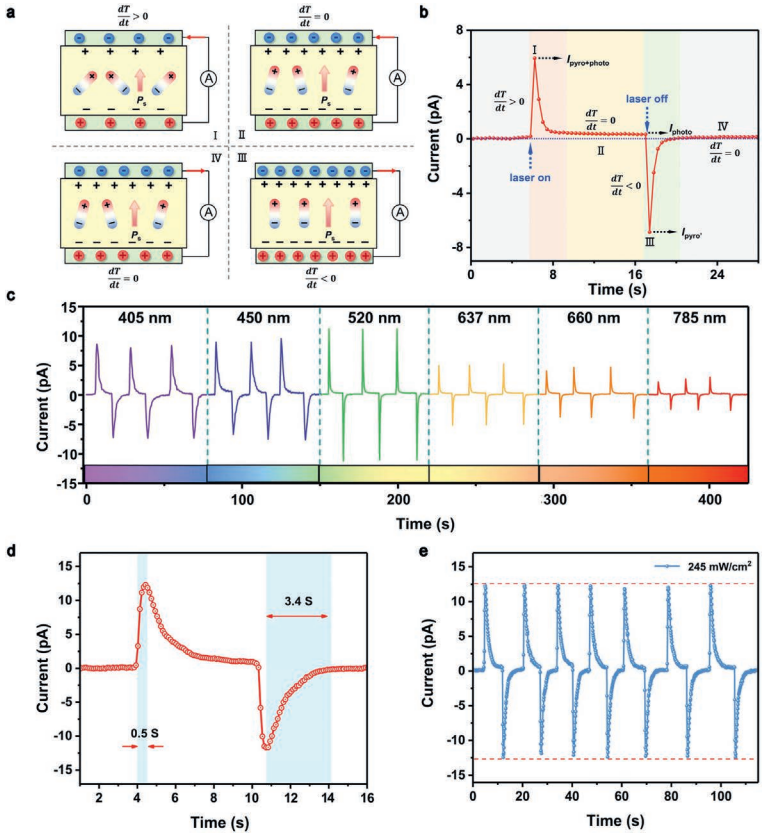


Fig. 4. (a) Working mechanism of pyro-phototronic effect. (b) Four stages of pyroelectric effect. (c) *I–t* curves of **1*R*** detector under different laser illumination (245 mW/cm^2). (d) The response time during one cycle. (e) Repeated switching cycles of the pyro-phototronic effect.

the temperature remains constant, leading to a stable plateau in the output current without the effect of pyroelectric, represented as I_{photo} ($dT/dt = 0$, stage 'II'). However, when the light is turned off, a reverse pyroelectric peak $I_{pyro'}$ is generated ($dT/dt < 0$, Stage III). In stage 'IV', the pyroelectric current gradually disappears as the temperature returns to room temperature ($dT/dt = 0$).

Fig. 4c depicts the *I–t* curves of **1*R*** within the spectral range from 405 nm to 785 nm, indicating the capability of a broadband response, which breaks the limit of optical bandgap. The curves reveal two distinct stages: initial sharp transient current peaks ($I_{pyro+photo}$), followed by a steady plateau (I_{photo}) without pyroelectric effect as the temperature remains constant. The current peak, a result of the combined BAPV and pyroelectric effects, shows a clear wavelength dependence and a high enhancement. Moreover, at zero bias, the peak pyroelectric current monotonically increases with increasing incident power (Fig. S10 in Supporting information). Since the temperature gradient increases with stronger light, it leads to higher densities of electrons and holes. These findings show that **1*R*** not only generates stable photovoltaic I_{photo} directly but also amplifies the response *via* the pyro-phototronic effect. The rising and falling components of the response time of **1*R*** inferred from single switching cycle are approximately 0.5 s and 3.4 s, respectively (Fig. 4d). Furthermore, the photostability of **1*R*** devices under 520 nm irradiation is depicted in Fig. 4e, demonstrating that the transient photoinduced pyroelectric current remains consistently stable without obvious degradation. These findings highlight the synergistic interaction between the BAPV and pyroelectric effects, offering a promising path toward advanced broadband self-powered photoelectric detection.

In summary, a pair of CHPs (S-α-MBA)$_4$Bi$_2$I$_{10}$ and (R-α-MBA)$_4$Bi$_2$I$_{10}$ have been synthesized, which crystallize in the chiral-polar space group of $P2_1$. This chiral-polar structure induces a superior bulk anomalous photovoltaic effect (BAPV), which exhibits an above-bandgap photovoltage extraordinary 15 V. As far as we know, this should be the first discovery of the BAPV effect in lead-free chiral hybrid perovskites. In addition, such BAPV effect gives rise to a distinctive pyro-phototronic effect, which further enables a highly enhanced self-powered detection with a broad response from 405 nm to 785 nm. Such photo-thermal coupling is capable of simultaneous multi-signal sensing and effectively enhances photoelectric response. These unique features establish a potential platform for optoelectronic applications, particularly in the field of photovoltaics.

Declaration of competing interest

The authors declare that they have no known competing financial interests or personal relationships that could have appeared to influence the work reported in this paper.

CRediT authorship contribution statement

Xin Dong: Writing – original draft, Data curation. **Zhijin Xu:** Formal analysis. **Jing Liang:** Formal analysis. **Tianqi Chen:** Investigation. **Junhua Luo:** Writing – review & editing. **Lina Li:** Writing – review & editing.

Acknowledgments

This work was financially supported by the National Natural Science Foundation of China (NSFC, Nos. 22322506, 22175177, 22193042, 22125110, 22122507, 21921001 and U21A2069), the NSF of Fujian Province (No. 2023J06052), the Key Research Program of Frontier Sciences of the Chinese Academy of Sciences (No. ZDBS-LY-SLH024).

Supplementary materials

Supplementary material associated with this article can be found, in the online version, at doi:10.1016/j.cclet.2025.111268.

References

[1] J.F. Scott, Science 315 (2007) 954–959.
[2] Y. Chen, C. Gao, T. Yang, et al., Chin. J. Struct. Chem. 41 (2022) 2204001–2204011.
[3] X. Yuan, J. Shi, Y. Kang, et al., Adv. Mater. 36 (2024) 2308726.
[4] H.S. Wu, B.T. Murti, J. Singh, P.K. Yang, M.L. Tsai, Adv. Sci. 9 (2022) 2104703.
[5] R. Mondal, M.A.M. Hasan, J.M. Baik, Y. Yang, Mater. Today 66 (2023) 273–301.
[6] L. Tang, W. Weng, H. Chen, et al., Adv. Funct. Mater. 33 (2023) 2214858.
[7] J. Chen, C.L. Hu, F. Kong, J.G. Mao, Acc. Chem. Res. 54 (2021) 2775–2783.
[8] C. Paillard, X. Bai, I.C. Infante, et al., Adv. Mater. 28 (2016) 5153–5168.
[9] H.Y. Ye, Y. Zhang, D.W. Fu, R.G. Xiong, Angew. Chem. Int. Ed. 53 (2014) 11242–11247.
[10] Y. Liu, W. Guo, L. Hua, et al., J. Am. Chem. Soc. 145 (2023) 16193–16199.
[11] L. Hua, L. Tang, Y. Liu, et al., Small 19 (2023) 2207393.
[12] R. Chakraborty, P.K. Rajput, G.M. Anilkumar, et al., J. Am. Chem. Soc. 145 (2023) 1378–1388.
[13] A.M. Glass, D. von der Linde, T.J. Negran, Appl. Phys. Lett. 25 (1974) 233–235.
[14] J. Carnicero, O. Caballero-Calero, M. Carrascosa, J.M. Cabrera, Appl. Phys. B 79 (2004) 351–358.
[15] J.E. Spanier, V.M. Fridkin, A.M. Rappe, et al., Nat. Photonics 10 (2016) 611–616.
[16] W.T.H. Koch, R. Munser, W. Ruppel, P. Würfel, Ferroelectrics 13 (1976) 305–307.
[17] S.H. Wemple, M. Didomenico, I. Camlibel, J. Phys. Chem. Solids 29 (1968) 1797–1803.
[18] S.Y. Yang, J. Seidel, S.J. Byrnes, et al., Nat. Nanotechnol. 5 (2010) 143–147.
[19] A. Bhatnagar, A.R. Chaudhuri, Y.H. Kim, D. Hesse, M. Alexe, Nat. Commun. 4 (2013) 2835.
[20] Y. Wang, L. Zhu, Y. Feng, Z. Wang, Z.L. Wang, Adv. Funct. Mater. 29 (2019) 1807111.
[21] Y. Zhang, J. Chen, L. Zhu, Z.L. Wang, Nano Lett. 21 (2021) 8808–8816.
[22] Y. Dai, X. Wang, W. Peng, et al., Adv. Mater. 30 (2018) 1705893.
[23] Z. Wang, R. Yu, X. Wang, W. Wu, Z.L. Wang, Adv. Mater. 28 (2016) 6880–6886.
[24] I.H. Park, K.C. Kwon, Z. Zhu, et al., J. Am. Chem. Soc. 142 (2020) 18592–18598.
[25] L. Li, W. Wu, D. Li, et al., CCS Chem. 4 (2022) 2491–2497.
[26] Z. Xu, X. Dong, L. Wang, et al., J. Am. Chem. Soc. 145 (2023) 1524–1529.
[27] B. Shi, P. Wang, J. Feng, et al., Nano-Micro Lett. 15 (2023) 3.
[28] P.J. Huang, K. Taniguchi, H. Miyasaka, J. Am. Chem. Soc. 141 (2019) 14520–14523.
[29] Y. Dang, X. Liu, B. Cao, X. Tao, Matter 4 (2021) 794–820.
[30] Y. Dong, Y. Zhang, X. Li, et al., Small 15 (2019) 1902237.
[31] J. Ma, H. Wang, D. Li, Adv. Mater. 33 (2021) 2008785.
[32] S. You, Z.K. Zhu, S. Dai, et al., Adv. Funct. Mater. 33 (2023) 2303523.
[33] T. Zhu, H. Wu, C. Ji, et al., Adv. Opt. Mater. 10 (2022) 2200146.
[34] J. Wu, S. You, P. Yu, et al., ACS Energy Lett. 8 (2023) 2809–2816.
[35] Y.L. Zeng, X.Q. Huang, C.R. Huang, et al., Angew. Chem. Int. Ed. 60 (2021) 10730–10735.
[36] T. Zhu, J. Bie, C. Ji, et al., Nat. Commun. 13 (2022) 7702.
[37] N. Ma, Y. Yang, Nano Energy 40 (2017) 352–359.
[38] W. Peng, X. Wang, R. Yu, et al., Adv. Mater. 29 (2017) 1606698.
[39] J. Tauc, Mater. Res. Bull. 3 (1968) 37–46.
[40] N. Dehnhardt, M. Axt, J. Zimmermann, et al., Chem. Mater. 32 (2020) 4801–4807.
[41] Z. Wang, R. Yu, C. Pan, et al., Nat. Commun. 6 (2015) 8401.
[42] S. Sahare, P. Ghoderao, M.K. Sharma, et al., Nano Energy 107 (2023) 108172.
[43] S. Tian, B. Li, Y. Dai, Z.L. Wang, Mater. Today 68 (2023) 254–274.